Atomic-scale understanding of the structural evolution of TiN/AlN superlattice during nanoindentation— Part 1: Deformation

Zhuo Chen[a], Yonghui Zheng[a,b], Yong Huang[a], Zecui Gao[c], Huaping Sheng[a], Matthias Bartosik[c,d], Paul H. Mayrhofer[c], Zaoli Zhang[a,*]

[a] *Erich Schmid Institute of Materials Science, Austrian Academy of Sciences, A-8700 Leoben, Austria*
[b] *Key Laboratory of Polar Materials and Devices (MOE), Department of Electronics, East China Normal University, Shanghai 200241, China*
[c] *Institute of Materials Science and Technology, TU Wien, A-1060 Vienna, Austria*
[d] *Department of Materials Science, Montanuniversität Leoben, Leoben, A-8700, Austria*

ARTICLE INFO

ABSTRACT

At present, the theoretical predictions of the mechanical properties of transition-metal nitride (TMN) superlattices (SLs) are primarily based on the intrinsic properties of perfect epitaxial nanolayers. However, due to a lack of understanding of the specific strengthening mechanism, the experimentally determined strength, e.g., hardness, of TMN SLs often deviates significantly from the theoretical predictions. Here, by coupling FIB (focused ion beam) sectioning with TEM, we observe the structural evolution of two representatives TiN/AlN SL coatings, i.e., a single-crystalline and a polycrystalline SL, under identical loads. We found that in comparison with the polycrystalline SL, the indented single-crystalline SL forms a larger 'intermixed' region, within which the layer structure transforms into a solid solution under loads. Close TEM characterization demonstrates that the single-crystalline SL deformation is of variety, including the distortion of SL interfaces, polycrystalline deformation (grain rotation) in solid solution, and SL slip deformation. By contrast, columnar grain boundary sliding is the primary deformation mechanism in the polycrystalline SL. And, a relatively large solid-solution zone in single-crystalline SL is attributed to the severe interfacial deformation. The current research unravels TMN SL deformation behavior at the atomic scale.

1. Introduction

Transition-metal nitride (TMN) coatings are of great importance for wear and tribological applications due to their extreme hardness and wear resistance. In the past, it has been realized that monolithic (single layer) TMN coatings can effectively protect cutting tools. However, with increasing demands from industry in terms of material hardness and toughness, multilayer architectures were used to further enhance the performance. It is currently known that when a multilayer with rock-salt/rock-salt superlattice (SL) structure is formed, the toughness and hardness are significantly increased [1–6]. The performance improvement can be attributed to the interface effect in nanoscale multilayer [7–12]. The outstanding toughness and hardness of the SL coatings are related to the interface, which include the effect of misfit dislocations, interface coherency strains, and the modulus difference between the layers materials [7,9,10,13].

Although numerous studies reported on the mechanical properties of TMN multilayer coatings, only a few works explored the deformation behavior of nitride multilayer coatings [14–17]. Since some films using different substrate materials or applying less severe deposition, TMN film tend to exhibit columnar grain structures. Previous work performed nanoindentation and nanoscratch experiments on TMN SL coatings and performed cross-sectional Scanning electron microscope (SEM)/Transmission electron microscope (TEM) characterizations [14–16,18,19]. These structures show that the plastic deformation of the polycrystalline coating is mainly due to the grain rotation and grain boundary sliding of the nanocrystals. The fracture modes were observed to initiate at the columnar boundaries and in the layers parallel to the interfaces [18]. However, the deformation and fracture behaviors of fully epitaxially stable single-crystal coatings with better mechanical properties are rarely reported. Since deformation and fracture behavior are important factors affecting the strength of TMN coatings and

---

* Corresponding author.
  E-mail address: zaoli.zhang@oeaw.ac.at (Z. Zhang).

their industrial applications, it is essential to characterize the microstructural evolution under mechanical loading.

Recent TEM research shows the deformation induced by nanoindentation can result in intermixing of the layer materials in a single-crystalline SL coating (with a small bilayer thickness, Λ=2.5 nm) [20]. However, how the microstructure affects the intermixing and deformation behaviors in TMN SL remains unexplored. In this work, at the atomic scale, we studied the deformation, fracture mechanisms, and the spatial distribution and extent of intermixed regions formed in a single-crystalline SL coating subjected to loads, and then compared the results to those of a polycrystalline SL coating. Using a C_S-corrected TEM, we found that the deformation of the single-crystalline SL coating is more complex, while the deformation of the polycrystalline coating is mainly governed by columnar grain boundary sliding. Hence, due to the difference in the deformation mechanisms, the single-crystalline SL exhibits a larger scale of solid solution zone than the polycrystalline SL.

2. Methods

2.1. Material fabrication

The TiN/AlN superlattice thin film ($\sim$ 1.5 µm total thickness, TiN $\sim$1.7 nm, AlN $\sim$0.8 nm) was synthesized using an AJA International Orion 5 lab-scale deposition system equipped with a computer-controlled shutter system. This bilayer period and layer distribution was chosen based on the previous study [21], showing that also the AlN layers fully crystallize to retain their metastable face-centered cubic (fcc) rock-salt (*rs*) structure. The reactive magnetron sputtering process was carried out at 700 °C (substrate temperature) in an Ar/N_2 mixed gas atmosphere with a total pressure of 0.4 Pa and an Ar/N_2 flow ratio of 7 sccm / 3 sccm. To avoid the intermixing of the two layer materials via excessive ion bombardment, we applied a rather low bias potential of –40 V (floating potential was –20 V) to the MgO (100) and Si (100) substrate, just enough to obtain a dense coating morphology. The three-inch Ti and two-inch Al targets were DC-powered setting constant target currents of 1.0 and 0.5 A, respectively. Further details can be found in Ref. [21]. To reduce the substrate effect and achieve better coating quality, the first layer of all coatings is TiN (approximately 5 nm thick). Except for the first TiN layer, other TiN layers maintain a constant thickness of 1.6 nm.

2.2. Material characterization

The nanoindentation was performed with an Ultra Micro Indentation System (UMIS, Fischer-Cripps Laboratories) equipped with a cube corner diamond tip using a maximum load of 100 mN and 150 mN. The maximum load depth is about 1.1 µm. The nanoindentation was carried out at a constant indentation strain rate (loading rate is about 10 mN/s). The FIB cutting positions are chosen near the tip of the indenter and cut along the ⟨100⟩ direction of the SL. During the FIB cutting, a protective layer of platinum with a thickness of about 2.0 µm was deposited on the area of interest. Two 6 µm deep trenches were made on either side of the selected region by coarsely milling at a current of 1.0 nA. After that, the exposed vertical faces of the specimen were coarsely polished by the ion beam using a current of 500 pA. An ion beam is used to cut off the entire bottom end and the vertical part. Finally, it is transferred and welded to a copper TEM grid for finely polishing under conditions of $\pm$ 2° and a beam current of 50 pA.

A 300 kV field emission TEM (JEOL ARM300F) equipped with double C_S-correctors were used in this study. Two windowless energy-dispersive X-ray spectroscopy (EDXS) detectors, each of which has an active area of 100 mm^2, are equipped on the microscope, which are very close to the specimen with a high solid angle (1.7 sr). A 200 kV field emission TEM (JEOL 2100F) equipped with an image-side C_S-corrector was used in the high-resolution TEM (HRTEM) study, which demonstrates a resolution of 1.2 Å at 200 kV. The aberration coefficients were set to be sufficient small under which the HRTEM images were taken under slightly over-focus conditions (close to the Scherzer defocus). Scanning TEM (STEM) images shown in this paper were recorded using a high-angle annular dark-field (HAADF) detector, with the detector inner angle/outer angle set to 54 mrad/144 mrad, respectively. Under these conditions, the STEM-HAADF contrasts are nearly proportional to the atomic number (Z-contrast image).

Electron energy-loss spectroscopy (EELS) spectra were recorded in two modes. The point spectra were recorded under the TEM-diffraction mode with a camera length of 25 cm with a dispersion of 0.2 eV per channel. The spectra were processed in Digital Micrograph (DM version 3.42, Gatan, USA). Firstly, the background was subtracted using the power-law model. For comparison, the spectra were then aligned to the N-K edge's onset to examine the variations of N-K and T-L edges, such as the chemical shift and shape change. EELS spectrum-images were acquired in the STEM mode using a dispersion of 0.2 eV per channel, a collection semi-angle of 10 mrad, and a convergence semi-angle of 2.5 mrad. The images were aligned to the N-K first peak and processed in DM. In the end, an energy difference map is obtained using the energy of the N-K first peak subtracting that of the N-K second peak, which can be used to distinguish the solid solution and layered region.

3. Results and discussions

3.1. As-deposited TiN/AlN structures

Superlattice coatings used in the present study are *rs*-TiN/*rs*-AlN deposited on MgO (100) and Si (100) substrates, where the AlN layer thickness is $\sim$ 0.8 nm and the TiN layer thickness is $\sim$ 1.7 nm. An overview of such epitaxial growth structure is displayed in the HAADF image (Fig. 1a). For SL grown on the MgO (100) substrate, since crystal structure and lattice constants between MgO and *rs*-TiN/*rs*-AlN are close, the coating has an entirely epitaxial single-crystalline structure (as seen in Figs. 1a-c). HRTEM (Fig. 1b) clearly reveals the atomic structure of a cubic-TiN/cubic-AlN a perfect epitaxial superlattice, where coating exhibits a single-crystalline structure. Measured interplanar spacings ($d_{(200)}$) in AlN and TiN layers are 2.0 Å and 2.1 Å, respectively, corresponding to the B1- AlN (with a lattice constant of 4.01–4.07 Å, Refs. [22,23]) and B1-TiN (with a lattice constant of 4.24 Å, JCPDF files: 38–1420). The analysis of the selected-area electron diffraction pattern (SAED) in Fig. 1c indicates that the projection direction is along cubic ⟨100⟩. Fig. 1c exhibits the superlattice spots (with some satellite spots), confirming that the periodic SL has a fully epitaxial growth of the cubic structures. In addition, a well-defined epitaxial SL (Figs. 1b-c) corroborates a thin AlN layer can be stabilized in the rock-salt structure.

For the coating grown on the Si substrate, epitaxial growth is not observed due to the presence of a native oxide on the Si (100) surface. The entire coating exhibits a polycrystalline microstructure with columnar growth features (as seen in Fig. 1d, low-magnification STEM-BF (scanning transmission electron microscopy bright-field) image, where the columnar grain boundaries are clearly visible). The width of the columnar crystals grown on the Si (100) substrate is 10–30 nm. The HRTEM observation (Fig. 1e, viewing on ⟨110⟩ direction) shows that the coating growth on the Si (100) substrate also has a rocksalt/rocksalt coherent interface structure within the individual columnar grains. However, the SAED over a larger region (Fig. 1f) presents an intense diffrac-
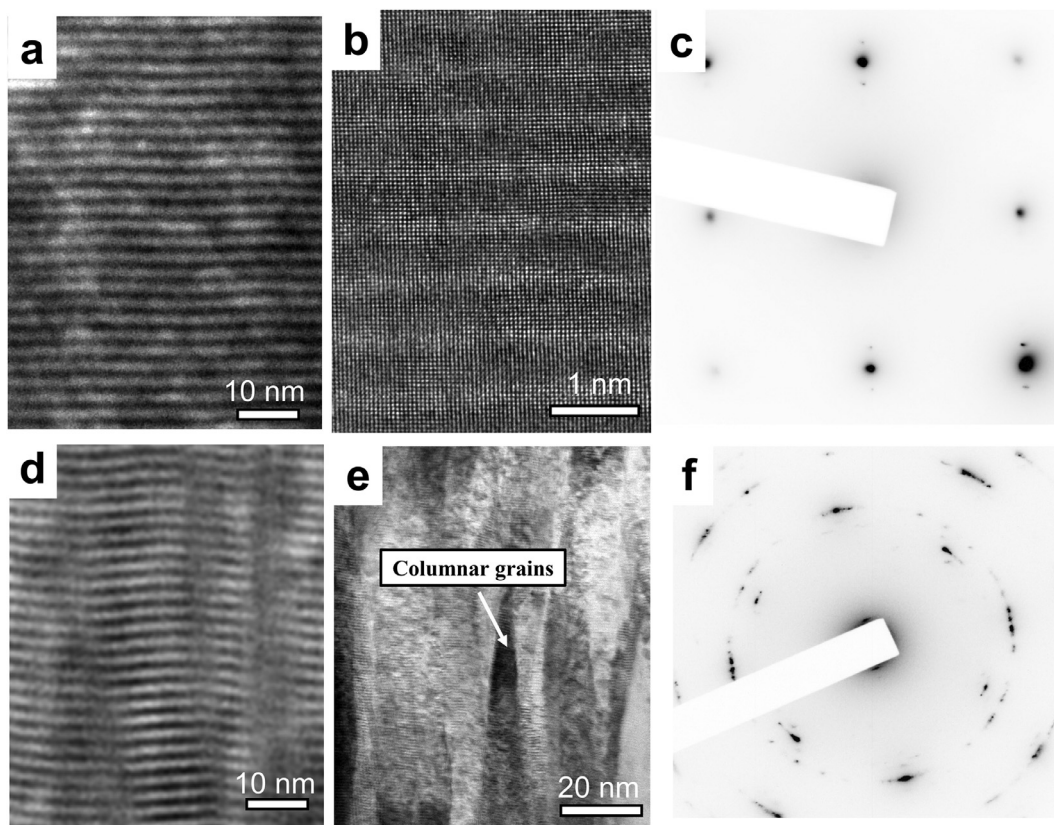
Fig. 1. a–c, as-deposited *rs*-TiN/*rs*-AlN superlattice on MgO (100) substrate. a, A cross-sectional HAADF image. b, A HRTEM image revealing the atomic structure of the as-deposited superlattice. c, A SAED pattern showing a spot pattern with satellite spots. D–f, as-deposited *rs*-TiN/*rs*-AlN superlattice on Si (100) substrate. Due to the natural oxidation of the Si surface, the coating is in fact grown on SiO_x. d, A STEM-BF image. e, A HRTEM image showing the atomic structure. f, A SAED pattern (obtained using an aperture size of about 500 nm) exhibiting a continuous ring pattern.

tion ring in ⟨200⟩ reflection, which proves most of the columnar grains with ⟨100⟩ growth direction, i.e., {200} texture. Notably, both SAED patterns (Figs. 1c and 1f) indicate that the crystal structures are cubic and no wurtzite AlN phase is present in any of the as-deposited coatings (no extra spots/rings appearing). This also signifies that both coatings have a rocksalt/rocksalt SL structure despite being single-crystalline and polycrystalline.

3.2. Intermixing behavior in single-crystalline and polycrystalline SL coatings

3.2.1. Intermixing in the single-crystalline SL coating

Fig. 2a shows a TEM BF (bright-field) cross-sectional view of the indented SL on MgO (100) substrate. When moving close to the surface of the residual impression, the layered morphology cannot be detected anymore, instead a solid solution of uniform composition forms (as seen in the HRTEM image). A HRTEM image (Fig. 2b) shows that the solid solution has a cubic structure projected along the ⟨100⟩ direction. Atomic-scale elemental mapping displayed in Fig. 2d reflects that superlattice interface intermixing has occurred at the area close to the indenter tip. Fig. 2d reveals that Al and Ti atoms reside at identical atom column positions, which finally confirms the formation of a cubic $Ti_{1-x}Al_xN$ solid solution from the *rs*-TiN/*rs*-AlN SL. However, at the region away from the impression surface, the coating still has a clear and perfect interface structure (Fig. 2c). Thus, we show that nanoindentation causes mechanical alloying in the TiN/AlN SL, ultimately resulting in the formation of a $Ti_{0.67}Al_{0.33}N$ single-phase solid solution under 100 mN. The solid solution forming process can be schematically illustrated in Fig. 2e, where Ti and Al atoms are randomly distributed in lattice. The chemical composition of this solid solution could be estimated from EDXS results, and it also fits the expected value, i.e., giving $x = 0.8/(1.7 + 0.8) = 0.33$ for $Ti_{1-x}Al_xN$ when mixing a 1.7 nm-thick TiN with a 0.8 nm-thick AlN.

After confirming that nanoindentation triggers interfacial mixing, here, we describe in detail the spatial distribution of the solid solution region at the tip position of the impression. The TEM-BF image in Fig. 3a displays the morphology of the indented coating (under 100 mN) in the impression tip region of the single-crystalline SL. At the position marked in frame (Fig. 3a), an HRTEM image was recorded, shown in Fig. 3b (atomic-resolution image projected in [100] direction). From the image, apparently, the lower part of the area has a layered structure while the upper part is a solid solution (with nearly homogeneous contrast, and no layered features). Therefore, according to Fig. 3b, intermixing of the two layers is observed in film regions up to ∼150 nm away from the impression surface. The intermixing phenomenon alters the electronic structure of TiN (or AlN) accordingly [24]. Fig. 3c shows the core-level EELS recorded from the solid solution (near the surface) and the superlattice regions (away from the surface). A close comparison shows that for the solid solution region, the width between the second peak and the first peak of N-K is smaller than that in SL region ($\Delta E_{N-k} \approx 7$ eV in the solid solution region and $\Delta E_{N-k} \approx 8.5$ eV in the SL region). Through the fine differences in the electronic structure, we are able to map the distribution of the solid solution. Fig. 3d shows such a map, i.e., the measured energy difference (ΔE_{N-k}) over a large area. The green-colored area in the upper part of the map corresponds to the solid solution zone, consistent with the HRTEM result, i.e., extending about ∼150 nm from the impression surface.
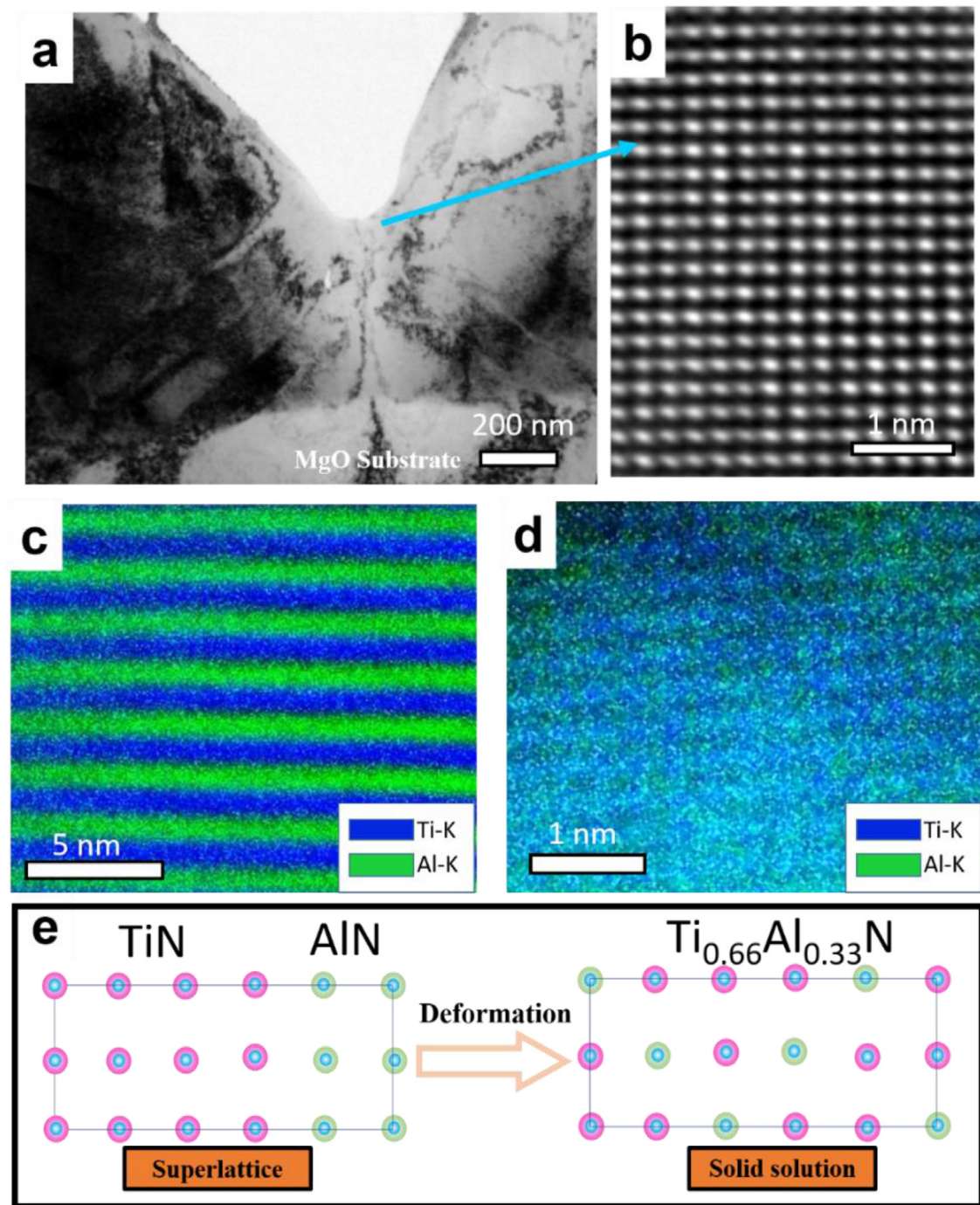
Fig. 2. a, A cross-sectional TEM-BF image of the indented (100 mN) *rs*-TiN/*rs*-AlN SL on MgO (100) substrate. b, A HRTEM image of the indented single-crystalline SL at the surface region. c, The elemental mapping (EDXS) at the position far away from the impression surface. d, Atomic-resolution elemental mapping in the surface region of the impression. e, Schematic atomic model illustration of the intermixing process, where the *rs*-TiN/*rs*-AlN SL evolves into a $Ti_{0.67}Al_{0.33}N$ solid solution.

3.2.2. Intermixing in the polycrystalline sl coating

(i) At the tip position of the impression

A TEM-BF image in Fig. 4a shows the morphology of the indented polycrystalline SL (film grown on the Si (100) substrate) at the tip region. In Fig. 4b, red marker locations indicate many areas with multilayer features. In contrast to the single-crystalline SL coating, we can easily detect multilayer features even at positions close to the impression surface, as shown in Fig. 4b. For the tip region, HRTEM observation (Fig. 4c) shows a solid solution feature, where no layer contrast is observed. More importantly, the observation position of Fig. 4c is only present very close to the tip surface. In comparison with the single-crystalline SL, the nanoindented polycrystalline SL forms a smaller 'intermixed' region. The EELS mapping result also more directly confirm these BF results. The energy difference mapping of the N-K edge (in Fig. 4d) shows that a 7 eV energy gap is detected only with a depth of 60 nm from the tip surface inwards. Thus, our EELS mapping results reveal that the extension of the solid solution in the polycrystalline SL coating at the tip region of the impression is much smaller than that in the single-crystalline SL coating (Fig. 3d).
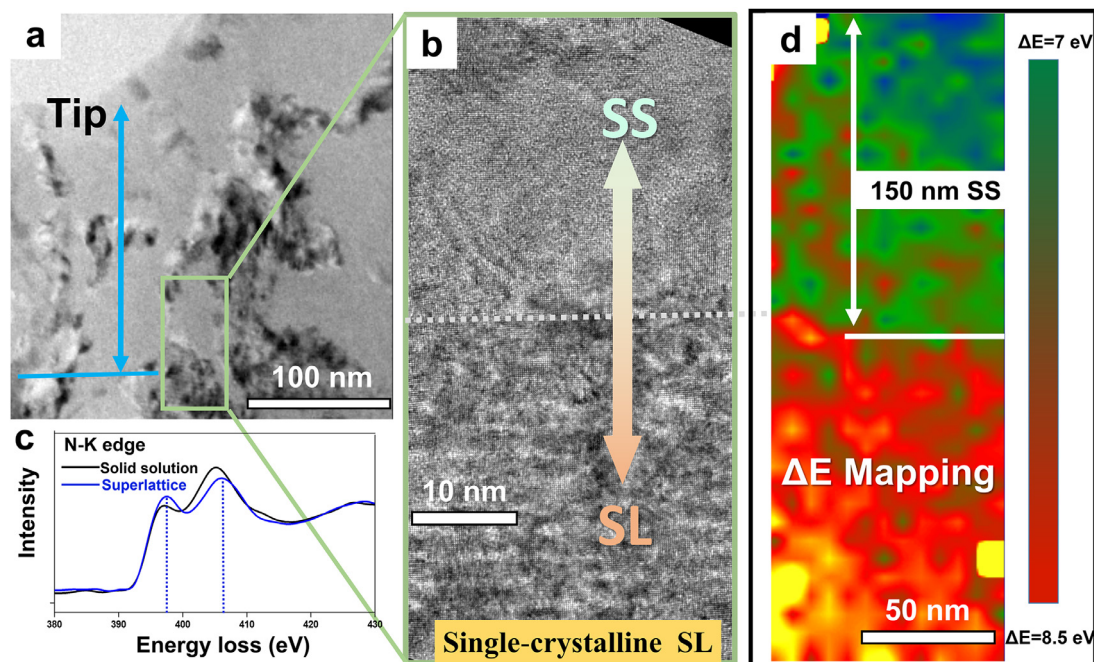
Fig. 3. a, A cross-sectional TEM-BF image of the indented single-crystalline SL at the tip position of the impression. b, A locally enlarged HRTEM image of the transition area (labeled in (a)) from the solid solution region to the SL region. c, EELS spectra (N-K edge) taken from near the surface (solid solution region) and a region away from the surface (SL region). d, EELS mapping using the energy difference (ΔE_{N-k}) between the second and the first peak of N-K edge. It is approximately 7 eV near the surface (green) and 8.5 eV far away from the surface (red). (For interpretation of the references to colour in this figure legend, the reader is referred to the web version of this article.)

(ii) Comparison of the edge position of the impression

Moreover, there is almost no solid solution formation observable for the area far away from the tip of the polycrystalline SL impression. A HAADF image in Fig. 5a shows the morphology of the indented polycrystalline SL coating at the edge region of the impression. The HAADF image (Fig. 5b, from position 'b') confirms that the surface area of the impression is full of the layer feature. Similarly, the impression surface also exhibits a superlattice structure at position 'c' further away from the tip (Fig. 5c). However, for single-crystalline SL coating, besides the tip region of the impression, intermixing also occurred at the edge region of the impression. The HAADF image presented in Fig. 5d shows an overview of the morphology of the indented coating at the edge region of the impression. In position 'e', the HAADF image (Fig. 5e) shows that the solid solution region (without the presence of layer contrast) is present up to ~50 nm away from the contact surface. As moving further away from the tip, i.e., 'f' position, the HAADF image (Fig. 5f) shows that the 'f' position hardly presents any solid solution feature, but only a severely deformed layer structure. Therefore, compared to the single-crystalline SL coating (Fig. 5e, 5f), almost no layer intermixing has occurred at the edge of the impression of the polycrystalline coating. As already seen, even a very smaller intermixed zone created by nanoindentation, hard to be seen by conventional SAED [16], could still be visualized by utilizing advanced TEM methods.

In summary, for the single-crystalline SL coating, we evidenced the solid solution formation, the spatial extension solid solution zone gradually decreases at the indenter impression edge when moving away from the tip. The largest volume of the solid solution zone was observed rightly underneath the impression tip.

3.3. Deformation and fracture behavior in the single-crystalline SL coating

3.3.1. Deformation in the solid solution region

TEM results (Figs. 1a-c) show that the as-deposited coating grown on the MgO (100) substrate is a [100] grown 'single-crystalline' film with a completely epitaxial superlattice structure. However, after nanoindentation, SAED patterns exhibits obvious grains rotation features in the solid solution region. Here, SAED patterns recorded from 4 different positions (marked in Fig. 6a) are displayed in Fig. 6b. These positions demonstrate diffraction patterns from two solid solution regions (positions **2** and **3**) and two superlattice regions (positions **1** and **4**), as also seen in inserted atomic-resolution HRTEM images (Fig. 6a). In position **2**, the 'ring' feature in SAED pattern is slightly enhanced compared to the as-deposited SL (Fig. 1c). However, more pronounced grains rotation features are observed in the tip region, and the corresponding SAED pattern presents the ring-like pattern (Fig. 6b, positions **3**). This strongly suggests more randomly oriented grains and more severe grain rotation behavior in the solid solution region. In addition, the series of dark-field images (Figs. 6c and 6d, using one portion of {200} reflection) also indicate that the nanocrystalline solid solution has a smaller grain size at the tip region, but a larger grain size further away from the tip region (Figs. 6e and 6f). Here, the created solid solution region (on MgO (100) substrate) in the single-crystalline SL by nanoindentation is mainly composed of equiaxed grains. Differently, the polycrystalline SL on the Si (100) substrate consists of columnar grains with a width of tens of nanometers and a texture characteristic (see Fig. 1d).

Through HRTEM, we further characterized the GB (grain boundary) atomic structures in the solid solution region. Fig. 7a shows a TEM-BF image of the surface region of the impression, where an equiaxed grain with 100 nm in size can be observed. In this grain, HRTEM observations (Figs. 6b-d, the atomic-resolution image projected in [100] direction) hardly show any multilayer features, indicating that such an equiaxed grain is a cubic $Ti_{0.67}Al_{0.33}N$ solid solution instead of the TiN/AlN SL. Further observations performed at different positions (Figs. 7b and c) reveal a 5°–18° tilt angle between the grain boundaries. There is even a sub-grain boundary comprised of an array of edge dislocations within such an equiaxed grain (Fig. 7d). The lattice rotation angle map of the corresponding
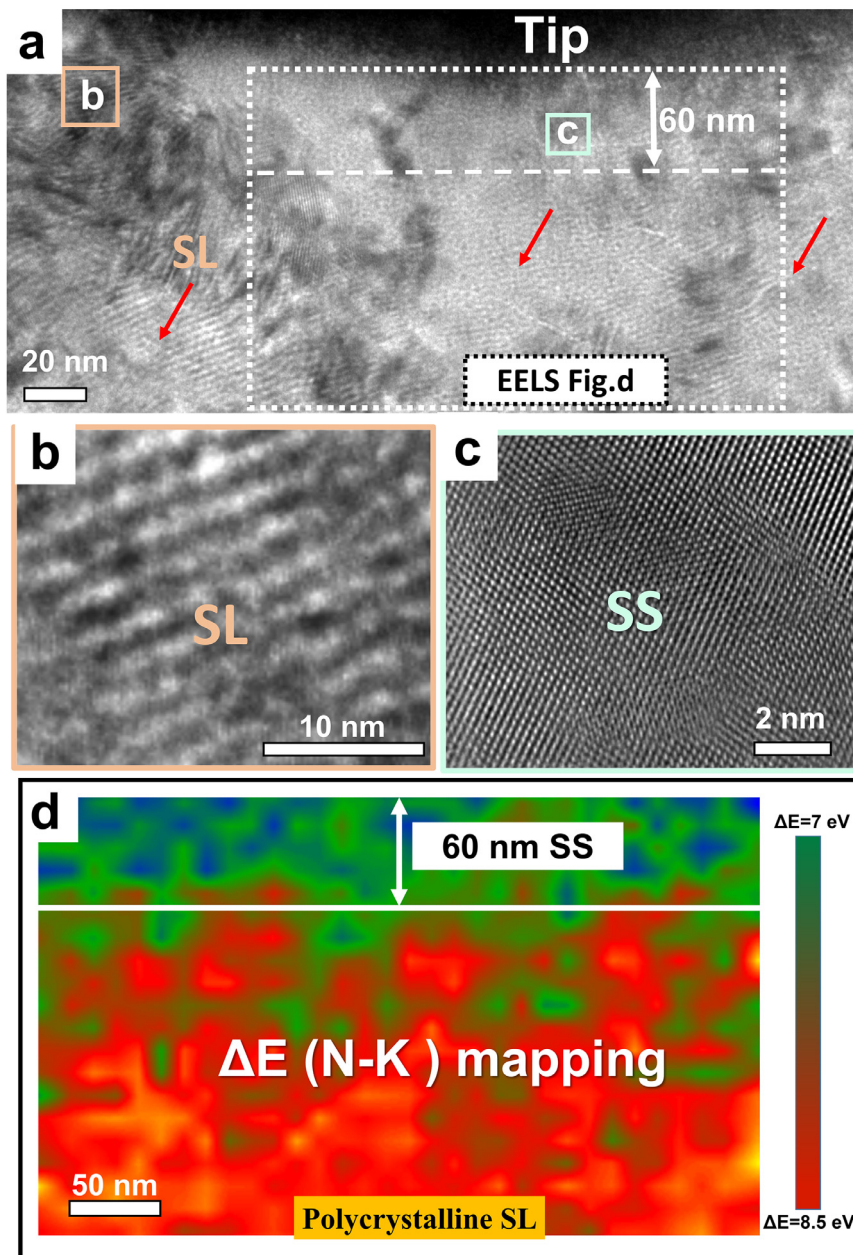
Fig. 4. a, A cross-sectional TEM-BF image of the indented polycrystalline SL at the tip position of the impression, where red labels show the position with multilayer features. b, Enlarged TEM-BF image (position marked in Fig. 4a). c, HRTEM observation at the tip position of the impression. d, EELS mapping of the energy difference between N-K second peak and N-K first peak. The energy difference on the surface (green area) is approximately 7 eV and far away from the surface (red area) is approximately 8.5 eV. (For interpretation of the references to colour in this figure legend, the reader is referred to the web version of this article.)

region reveals that the tilt angle across the boundary is about 2–5° (as shown in Fig. 7e).

For the contact surface of the indenter, we believe that the total volume of the solid solution area increases as the indentation depth increases. This is because the multilayer region accompanied with high dislocation density will continue to transform into a solid solution with proceeding indentation, and finally form a large solid solution region as observed. Previous molecular dynamics (MD) simulation results [20] show that when the load depth is about 3 nm, a solid solution has already been formed. This indicates that the solid solution behavior occurs in the very early stage of the indentation event. After the solid solution is formed, it has the potential to lower the resistance to shear and favors dislocation glide by modifying the electronic effects (high valence electron concentration) and bonding characteristic [25,26]. Since intragranular dislocations are easily redistributed in a solid solution re-

gion (from dislocation accumulation before intermixing), the deformation in solid solution region will be mediated by grain rotations, including the structural evolution from the initial larger solid solution grains (come from the SL intermixing)—sub-grainboundaries—small-angle grain boundaries—large-angle grain boundaries. In the tip region of the impression, where the local stress is large, more serious rotation deformation in the nanocrystalline solid solution takes place. This statement is also confirmed by the fact that the tip of the impression possesses much more refined grains and the presence of a larger fraction of high-angle grain boundaries (as seen in the SAED, i.e., Fig. 6b and Supplementary Figs. S1).

3.3.2. SL interface distortion

At the edge area of the impression (Fig. 8a), we observed a special superlattice zone with severely distorted interfaces in the single-crystalline SL. The HAADF image (Fig. 8b) shows the
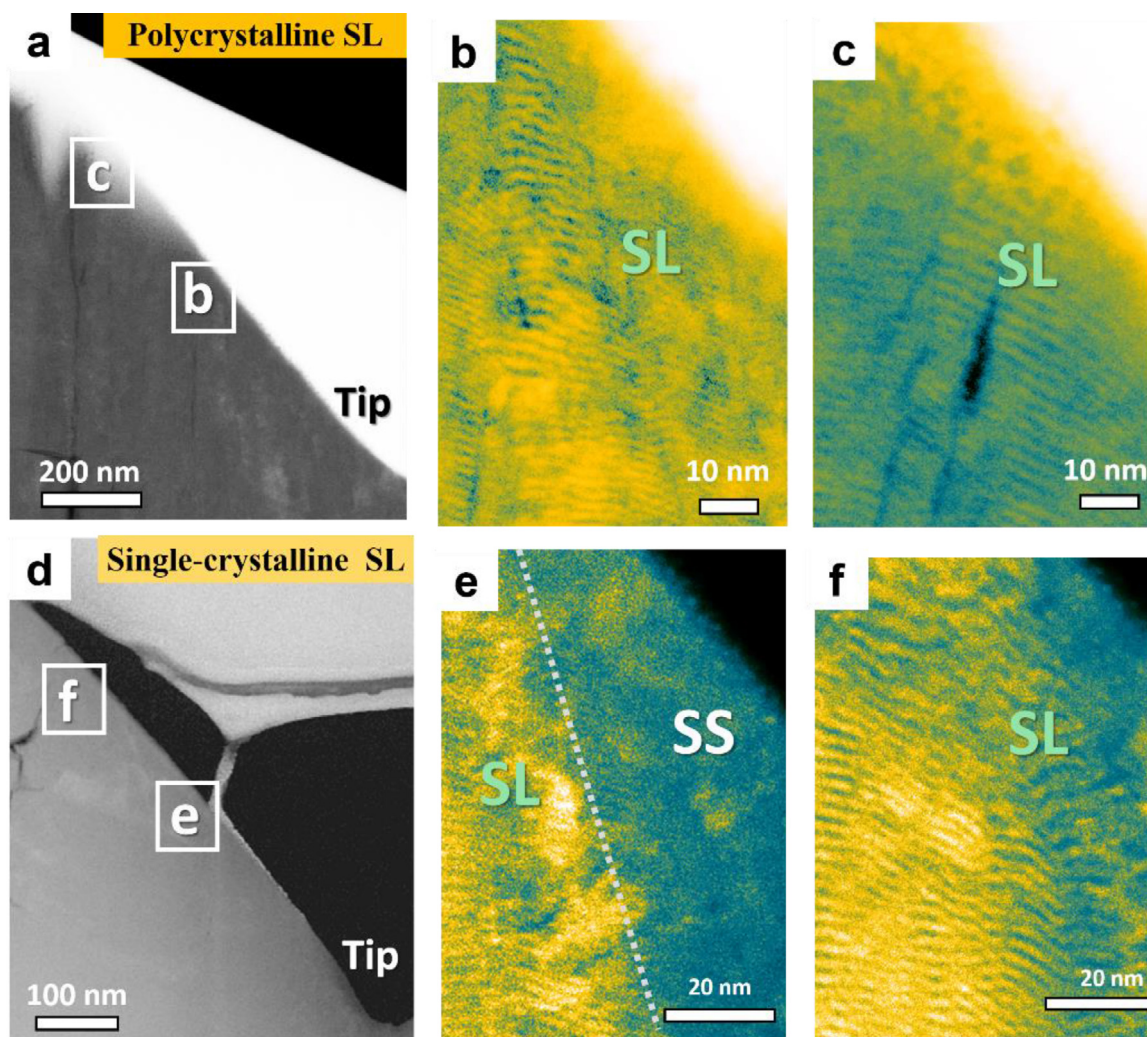
Fig. 5. a, STEM-HAADF image of the indented polycrystalline SL near the edge position of the impression. b and c, Higher magnification HAADF images taken from different locations (as framed in a) showing the distribution of the $Ti_{0.67}Al_{0.33}N$ solid solution zone at the edge position of the impression. d, STEM-HAADF image of the single-crystalline SL near the edge position of the impression. e and f, Higher magnification STEM-HAADF images show the distribution of $Ti_{0.67}Al_{0.33}N$ solid solution on the different edge positions of the impression (as framed in d). 'SS', 'SL', and dotted lines stand for $Ti_{0.67}Al_{0.33}N$ solid solution, TiN/AlN superlattice, and boundaries in-betweens.

morphology of such distorted interfaces, where the interfaces become rather rough and disrupted, and the layer morphology locally exhibits prominent bends and distortions. At the edge of the impression, this interface distortion structure is mainly distributed near the contact surface of the indenter, further deep inside the coating, the 'flat' interface morphology still retains (not shown here). Looking specifically at the structure of the distorted interfaces zone, we observed that the SL here was fragmented into small pieces (Fig. 8c). Compared to the solid solution region, no obvious grain boundary structure between these fragments is found. And, the HRTEM image (Fig. 8d) clearly shows very high densities of edge dislocations present in these distorted interface regions. The dislocations are present not only near the TiN/AlN interfaces but also inside the individual TiN or AlN layer. Thus, these TEM observations unravel that the dislocation densities in the interface distortion region are greatly increased as compared to the as-deposited SL interfaces.

However, we hardly observed the severe interface distortion and bending rightly beneath the tip region of the impression. In Fig. 8e, the contact surface of the impression tip is a solid solution without any layered features (not shown here). Along the compression direction of the indenter, we only observed a 'flat interface'

and no distorted interface distribution (as seen in Fig. 8f). Based on the observations, we may simply conclude that SL interface distortions mainly appear at the indenter edge where the shear deformation is dominant, while it is barely distributed at the tip area where the local stress is more concentrated.

3.3.3. SL slip deformation

The deformation of single-crystalline TiN coating has been studied in the past either by TEM or by calculating the crystallographic anisotropy using Schmid's law [27]. The primary slip system for dislocation glide in TiN crystals has been identified. Slip primarily occurs on {110} planes along the ⟨110⟩ directions [27,28]. Our results evidence that slipping, similar to TiN single-crystals, can also be found in single-crystalline TiN/AlN SL coating that occurs at the SL region away from the impression surface and gradually approaching to the MgO substrate.

For a better understanding of the scale of the slip deformation, we also characterized the slip deformation under 100 mN and 150 mN loads (as seen in Fig. 9a and 9b). For the 100 mN-indented sample (Fig. 9a), several slip lines (6 slip lines) along the ⟨110⟩ direction are observed, and the distance between these slip lines is about ~100–150 nm. Under a larger indent load (150 mN,
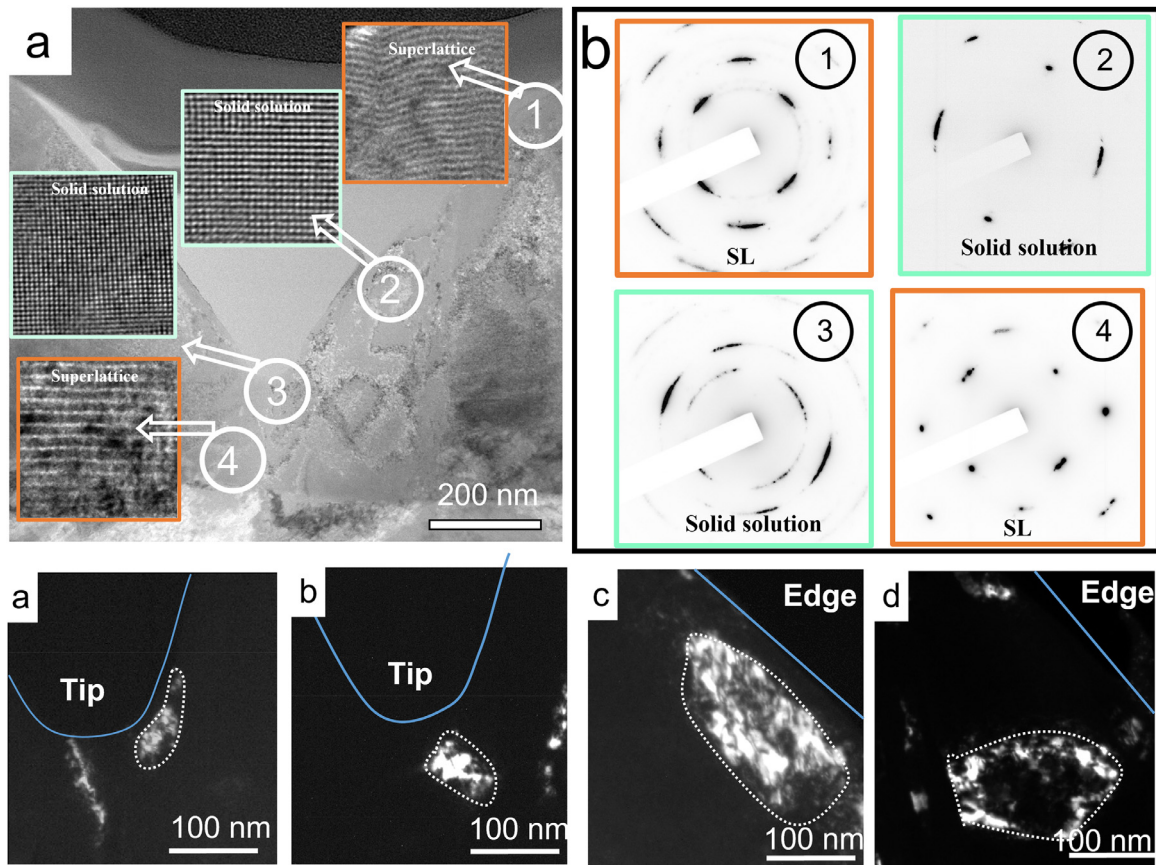
Fig. 6. a, TEM-BF image of the indented single-crystalline SL. Inserted images showing HRTEM images taken from the labeled positions 1–4. b, Corresponding SAED results in positions 1–4. The diameter of the selected area aperture used is about 150 nm. Note the differences in the SAED patterns of the different locations. c-f, TEM dark-field images were taken from the tip of the impression (c and d) and the edge area (e and f) using $g=$ [200] reflections of the cubic. In Fig. 6b, the enlarged image (position 4, inset) indicates the extra spots, confirming the presence of periodic SL structure. Please note that in Position 1, the faint diffractions due to the surface protective layer (Pt from FIB) are accidentally located at the satellite spot positions.
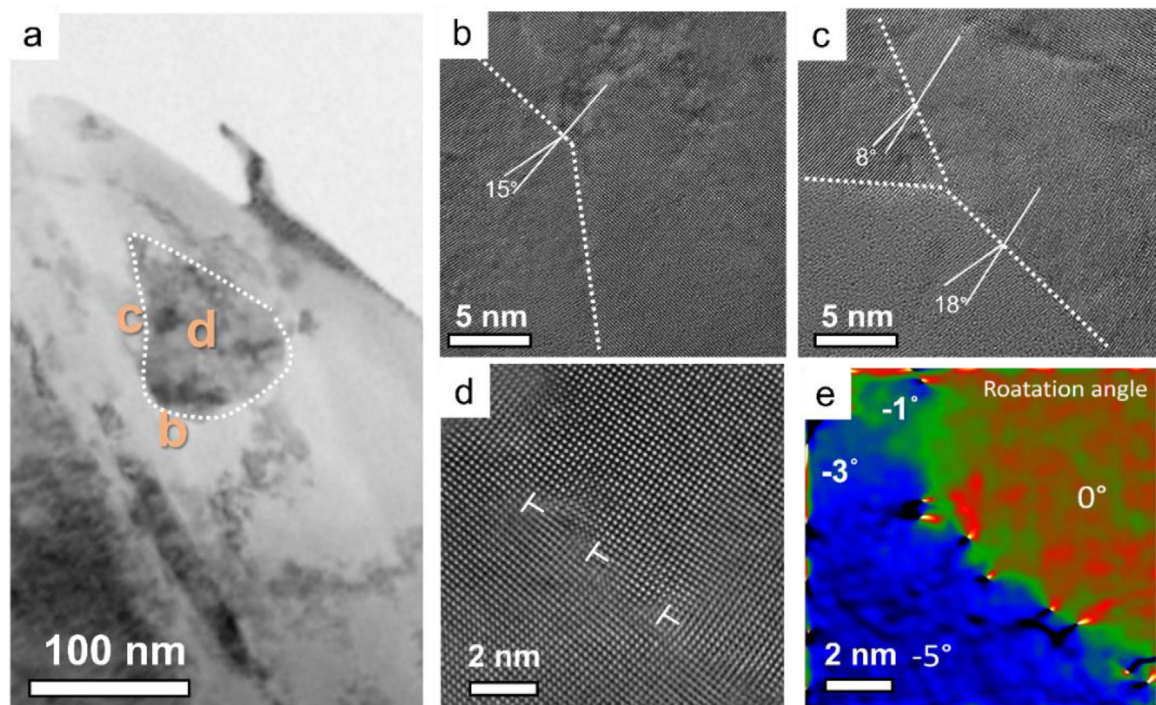

Fig. 7. a, A TEM-BF image of a nanocrystalline solid solution zone (one grain is indicated) in the indented single-crystalline SL. b-d, HRTEM images of grain boundary structures taken from different positions (labeled in a) in the solid solution zone. e, Lattice rotation angle mapping of d. Different boundaries labelled by dotted lines or an array of dislocations are clearly visible.
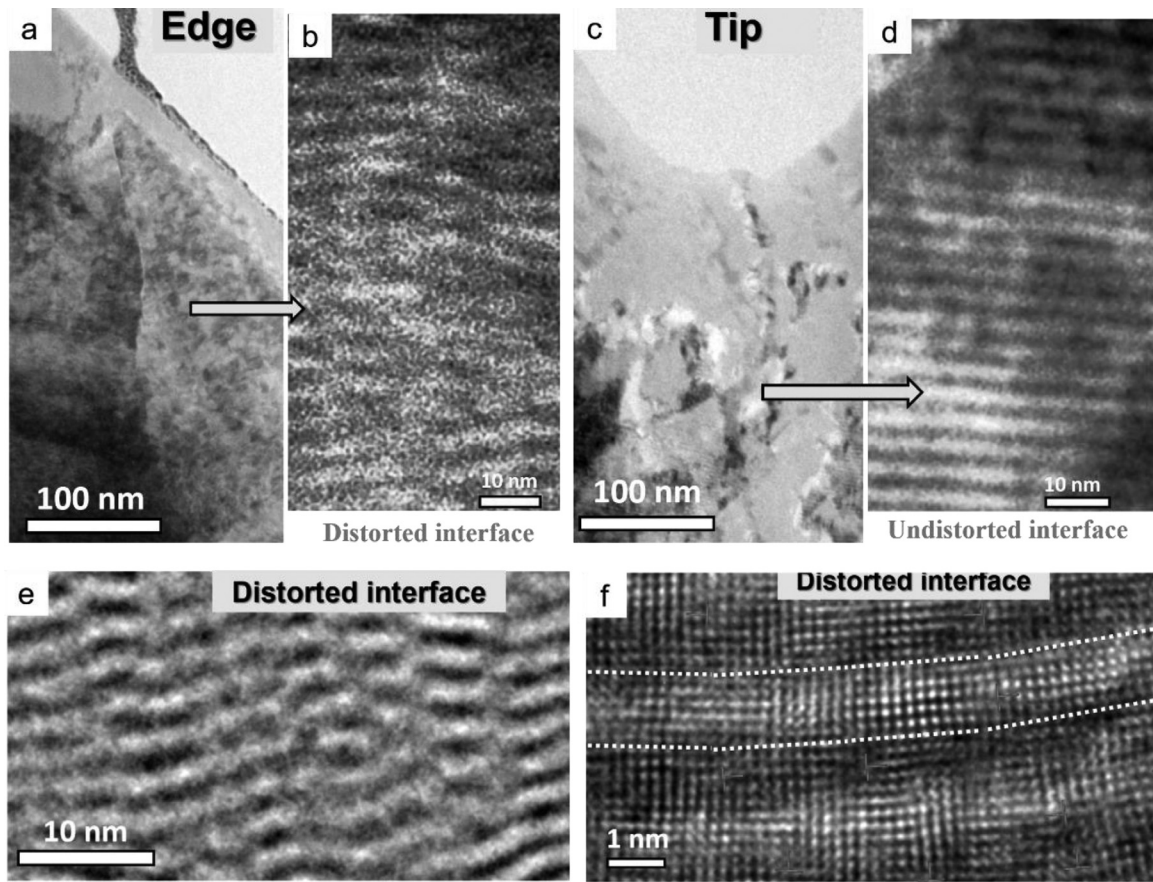
Fig. 8. a, A cross-sectional TEM-BF image of the indented single-crystalline SL at the edge position of the impression. b, A STEM-HAADF image recorded from one position in a showing the morphology SL interfaces. c, A TEM-BF image of the distorted. d, HRTEM observation result of the interface distortion region. e, A cross-sectional TEM-BF image of indented single-crystalline SL at the tip position of the impression. f, the STEM-HAADF observation results from one corresponding position in e.
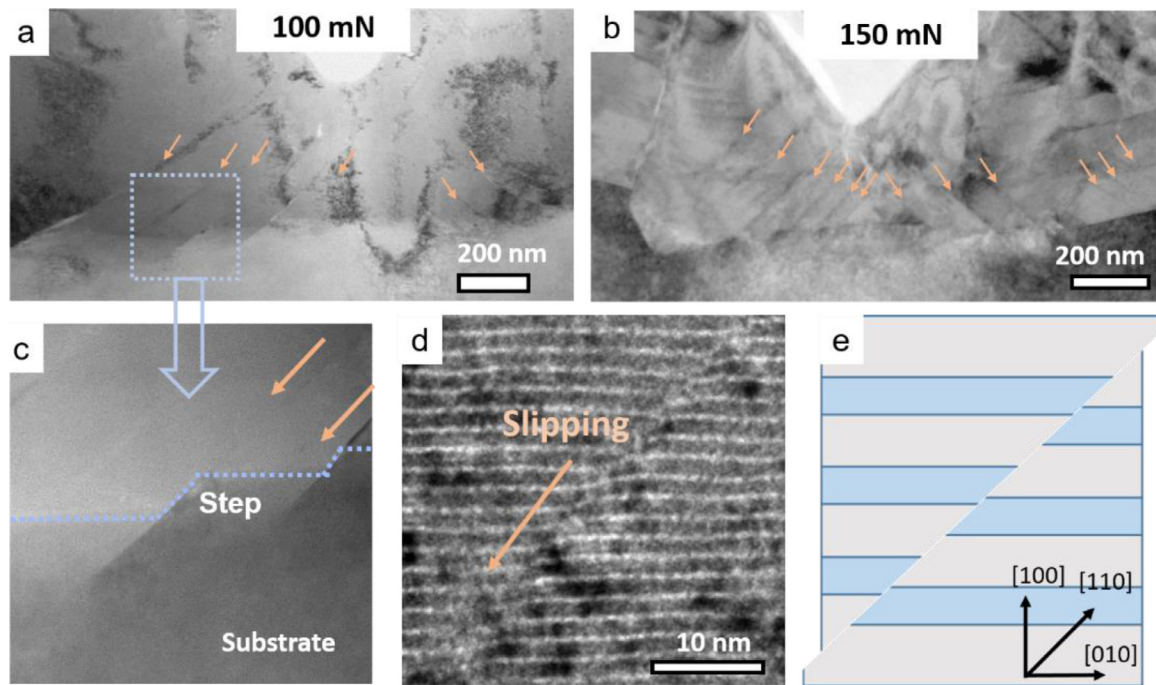

Fig. 9. a, b, Overall morphology of the single-crystalline SL under 100 mN and 150 mN load, respectively. The arrows indicate slip lines. c, The STEM-HAADF results of the corresponding area in a. d, The high magnification TEM BF image shows the slip deformation along the ⟨110⟩ direction. e, A schematic diagram of SL slip direction.
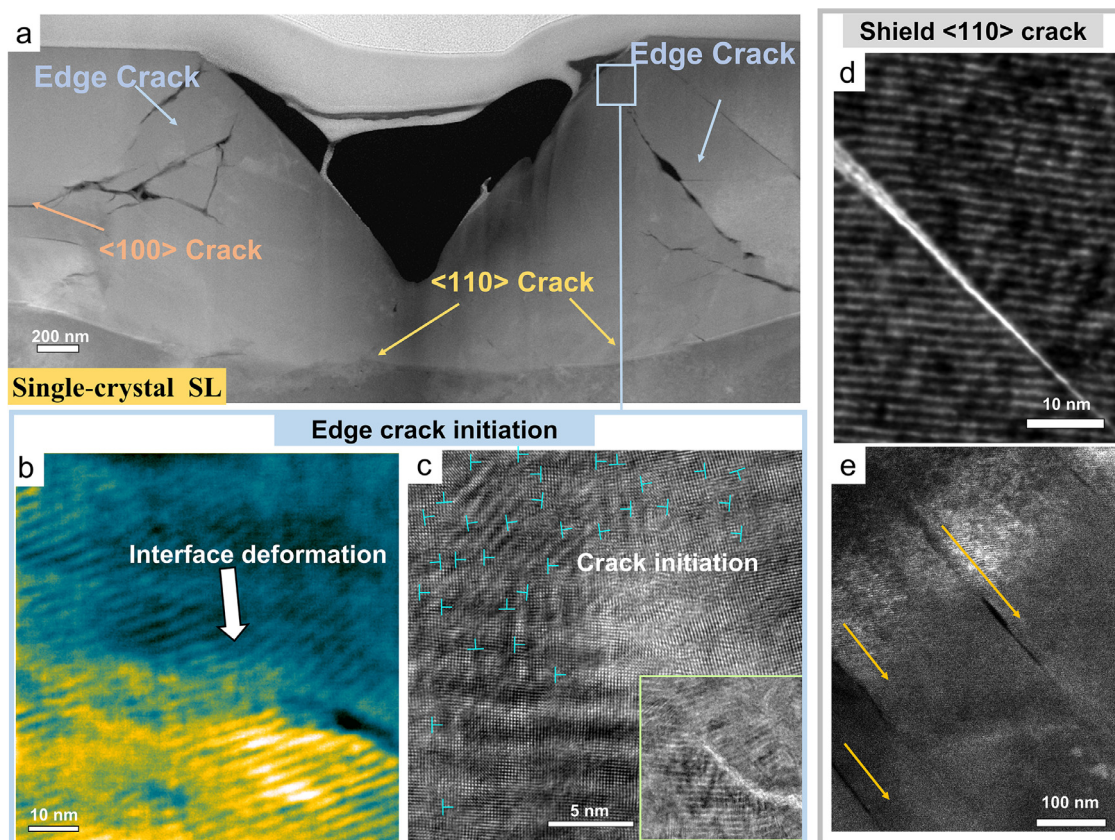
Fig. 10. a, Overview morphology (STEM-HAADF image) of the indented single-crystalline SL (under 100 mN) some cracks along different directions are clearly visible. b, detailed STEM-HAADF observation of the crack initiation region at the edge position of the impression. c, HRTEM observation near the crack initiation. The inserted image shows the low-magnification morphology of the crack tip area. ᴅ-e, TEM-BF and STEM-HAADF observations of the fracture behavior in the main slip direction (<110> direction).

Fig. 9b), the scale of slip deformation is greatly increased. Comparatively, the TEM BF result (Fig. 9b) shows that the density of the slip lines at 150 mN (12 slip lines are observed) is significantly higher than that under 100 mN. In addition, the step height on the interface under different loads is also different. Fig. 9c (100 mN) shows the TEM-BF image taken near the substrate area, and an obvious shearing step can be found, where the step height is ∼30 nm. For the 150 mN-indented sample, the step height can reach up to ∼100 nm. Detailed high-magnification TEM-BF observation (Fig. 9d) confirmed the sliding deformation in the 45° direction of the SL interface, i.e., sliding deformation of the SL along the ⟨110⟩ direction. Meanwhile, the interfaces near the SL slip lines are very flat and smooth, as shown in Fig. 9d A schematic drawing illustrates the sliding process happening along the 45° direction relative to the SL interface (Fig. 9e).

In short, strains generated by nanoindentation in the single-crystalline SL could be released by various deformation mechanisms, depending on the locations relative to the indenter. These cover: a polycrystalline deformation mode (i.e., grain rotation) in the solid solution area just rightly at the tip, distortion of the SL interfaces at the edge of the impression, and SL slip deformation far away from the contact surface.

3.3.4. Fracture in the single-crystalline SL coating

The fracture behavior of the single-crystalline SL coating was closely observed after an indent was made using a sharp cube-corner indenter and a maximum load of 100 mN. Low-magnification HAADF observation (Fig. 10a) shows that cracks are mainly located in the SL area at the edge of the impression, while the solid solution area (at the tip and edge region of the impres-

sion surface) barely exhibit any cracks. At the edge of the impression, cracks have an irregular extending direction, e.g., parallel to the interface direction, perpendicular to the interface direction, or along the interface direction at 45°, etc. For the cracks at the impression edge, Fig. 10b through 10c depicts the specific microscopic interface morphology of the initiation area. The interfaces in these areas are severely deformed. HRTEM observation on the corresponding position (Fig. 10c) shows the microscopic morphology of the crack initiation area, where the interface in the front of the crack demonstrates significant distortions and a very high dislocation density (as indicated). Accordingly, we can confirm that the initiation of cracks can be related to the accumulation of dislocations at the SL region of the impression edge. In addition to the edge of the impression, some micro-cracks along the sliding direction are observed. These cracks are titled 45° with respect to ⟨100⟩ growth direction (as seen in Fig. 10d), i.e., cracks along the ⟨110⟩ direction. But these ⟨110⟩ direction cracks can only travel a limited distance, i.e., only about 100 nm into the coating, as shown in Fig. 10e.

In a nutshell, for the single-crystalline SL, cracks mainly initiate and propagate in the SL area that is enriched with the distorted interfaces. Both the solid solution zone and the SL area without interface distortions may effectively prevent crack initiation and propagation.

3.4. Deformation and fracture behavior in polycrystalline SL coating

Polycrystalline SL coating has completely different deformation and fracture mechanisms from the single-crystalline SL coating. Fig. 11a shows the overall morphology of the polycrystalline SL
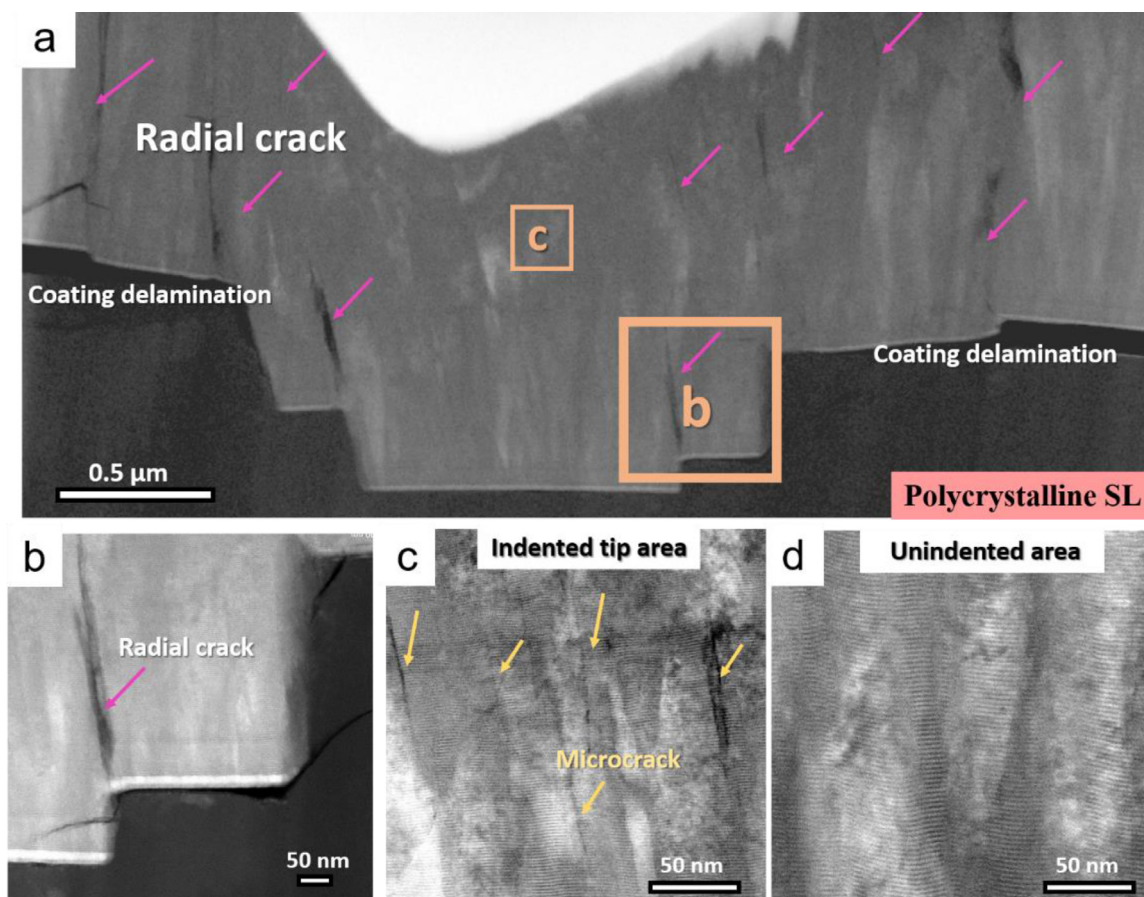
Fig. 11. a, Overall morphology (STEM-HAADF) of the indented polycrystalline SL (under 100 mN) with radial cracks being clearly visible. b and c, Detailed STEM-HAADF observation result of the corresponding areas in a (framed). d, STEM-HAADF observation result of the area not affected by the indentation.

coating after nanoindentation. For the fracture, Fig. 11a depicts that polycrystalline SL coating mainly has radial cracks perpendicular to the interface direction. These macroscopic cracks may propagate a distance of hundreds of nanometers (about 410 ~940 nm) and reach the substrate interface (as seen in Fig. 11b). Meanwhile, the indentation can cause the coating to delaminate from Si substrate (Fig. 11b). In addition to the obvious macroscopic fractures, a high density of micro-cracks is also observed at the tip area of the impression (Fig. 11c). These high-density micro-cracks are found only at the tip area of the impression, barely visible away from the tip (Fig. 11d, crack-free). TEM image shows that the shear steps appear along the column's slide direction, and continue to the coating-Si substrate interface. The formation of radial cracks can be considered as the gap between two adjacent steps be fractured by imposing more restraint and restraint on the columnar slip at the coating-substrate interface [16]. Furthermore, due to the lack of an epitaxial relationship and more unstable Si-N bonding [29], the film on the Si substrate easily delaminates and causes catastrophic failure.

As seen in Fig. 11a, the deformation in the polycrystalline SL coating is mainly governed by the sliding of columnar grain boundaries [30]. The strains generated by nanoindentation are released through shearing of the columnar grains. In Fig. 11a, the obvious sliding steps at the height of 80–350 nm in the substrate are observed, and the SL films are pushed into the substrate. Compared with the sliding step near the coating substrate of the single crystal SL (100 mN in Fig. 9a, and 150 mN in Fig. 9b, where comparably small steps), the polycrystalline coating demonstrates larger sliding steps. Since significant energies could be dissipated by sliding

deformation, this actually prevents large-scale interface distortion and alloying in the polycrystalline SL coating.

For columnar grain boundaries, it is easy to cause stress concentration during deformation. As a result, the interface distortion, dislocation accumulation and SL alloying can occur only near the GBs or crack regions. Fig. 12a depicts the multilayer morphology near the impression tip. Near the columnar GB (Fig. 12b), SL interfaces are obviously bent and distorted. Furthermore, the interface of the local area adjacent to the GB is not very clear (near yellow label), which implies a mixing phenomenon. However, a few nanometers away from the columnar GB (Fig. 12c), the interfaces are sharp, un-deformed and present a 'flat' feature. In addition to the GB region, a small-scale interface distortion and SL intermixing can also be observed near the cracks. Fig. 12d shows the morphology of one crack nearby in the columnar crystals. HRTEM observations (Fig. 12e) reveal that no layer features near the crack (as marked by the dotted-line area). This proves that there exists a localized intermixing zone adjacent to the crack. Meanwhile, HRTEM observations (Fig. 12f) also reveal the interface distortion near the crack and a high amount of dislocations (as indicated). However, it should be mentioned that the high dislocation density and the interface distortions appear only in the very vicinity of the crack. About 5 nm away from the crack (Fig. 12g, position 'g' labeled in Fig. 12d), the interfaces exhibit a perfectly coherent state and maintain a low dislocation density. Therefore, these atomic-resolution observations indicate that the interfacial intermixing and interfacial deformation in polycrystalline SL still occur locally (near the crack or GB) but with a low scale.
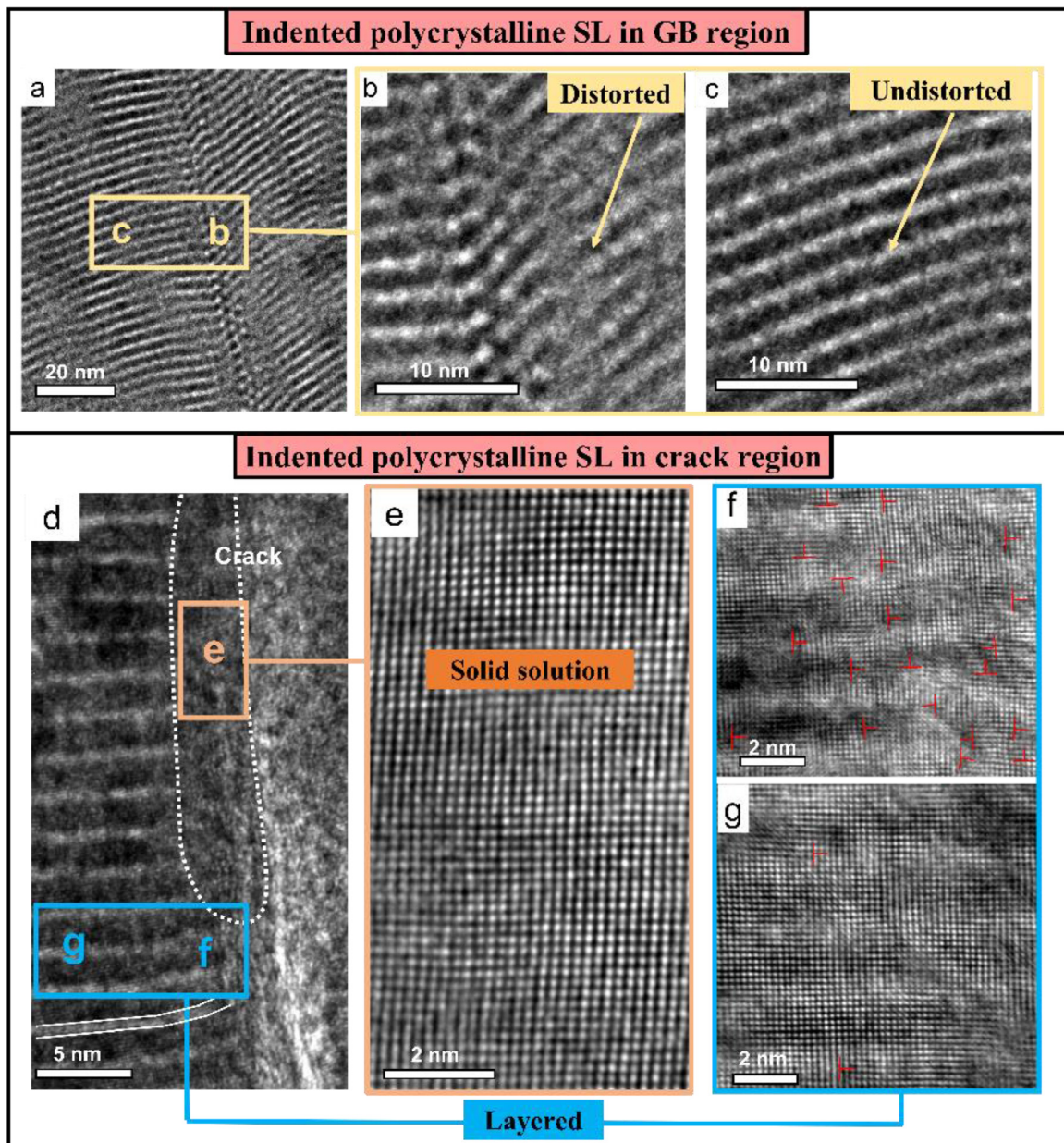
Fig. 12. a-c, A TEM-BF image of the indented polycrystalline SL from the columnar GB region. d, A TEM-BF image of near radial crack front in the polycrystalline SL. The white marked area demonstrates no multilayer feature is present next to the front of the crack. e-g, HRTEM observation results of the corresponding areas marked in d without layered features (e) and with layered features (f, g).

4. Conclusions

The microstructures of nanoindented single-crystalline and polycrystalline TiN/AlN SLs (Λ=2.5 nm) were intensively investigated using Cs-corrected TEM and FIB sectioning. Through atomic-scale TEM observations, we observe a variety of deformation mechanisms to be active in the single-crystalline SL coating, including SL interface distortion, SL slip deformation, solid solution formation and polycrystalline grain rotation in the solid solution. However, columnar grain boundary sliding along the loading direction is the predominant deformation mechanism in the polycrystalline SL coating, and interface distortion and SL alloying occur only locally in regions near the columnar grain boundaries. Hence, due to the difference in the deformation mechanisms, the single-crystalline SL exhibits a larger scale of solid solution than the polycrystalline S. For single-crystalline SL, the largest volume of the solid solution zone was observed rightly underneath the impression tip, and the spatial extension of this zone gradually decreases at the indenter's impression edge when moving away from the tip.

Supplementary materials

Supplementary material associated with this article can be found, in the online version, at doi:10.1016/j.actamat.2022.118008.

References

[1] H.A. Jehn, Multicomponent and multiphase hard coatings for tribological applications, Surf. Coat. Technol. 131 (1) (2000) 433–440.

[2] B.O. Postolnyi, V.M. Beresnev, G. Abadias, O.V. Bondar, L. Rebouta, J.P. Araujo, A.D. Pogrebnjak, Multilayer design of CrN/MoN protective coatings for enhanced hardness and toughness, J. Alloys Compd. 725 (2017) 1188–1198.

[3] H. Holleck, V. Schier, Multilayer PVD coatings for wear protection, Surf. Coat. Technol. (1995) 328–336 76–77.

[4] S.J. Bull, A.M. Jones, Multilayer coatings for improved performance, Surf. Coat. Technol. 78 (1) (1996) 173–184.

[5] G.S. Kim, S.Y. Lee, J.H. Hahn, S.Y. Lee, Synthesis of CrN/AlN superlattice coatings using closed-field unbalanced magnetron sputtering process, Surf. Coat. Technol. 171 (1) (2003) 91–95.

[6] J. Lin, J.J. Moore, B. Mishra, M. Pinkas, W.D. Sproul, Nano-structured CrN/AlN multilayer coatings synthesized by pulsed closed field unbalanced magnetron sputtering, Surf. Coat. Technol. 204 (6) (2009) 936–940.

[7] R. Hahn, M. Bartosik, R. Soler, C. Kirchlechner, G. Dehm, P.H. Mayrhofer, Superlattice effect for enhanced fracture toughness of hard coatings, Scr. Mater. 124 (2016) 67–70.

[8] J. Buchinger, N. Koutná, Z. Chen, Z. Zhang, P.H. Mayrhofer, D. Holec, M. Bartosik, Toughness enhancement in TiN/WN superlattice thin films, Acta Mater. 172 (2019) 18–29.

[9] J.S. Koehler, Attempt to design a strong solid, Phys. Rev. B 2 (2) (1970) 547–551.

[10] N. Koutná, P. Řehák, Z. Chen, M. Bartosik, M. Fallmann, M. Černý, Z. Zhang, M. Friák, M. Šob, P.H. Mayrhofer, D. Holec, Correlating structural and mechanical properties of AlN/TiN superlattice films, Scr. Mater. 165 (2019) 159–163.

[11] P.C. Yashar, W.D. Sproul, Nanometer scale multilayered hard coatings, Vacuum-Vacuum 55 (3) (1999) 179–190.

[12] R.G. Hoagland, R.J. Kurtz, C.H. Henager, Slip resistance of interfaces and the strength of metallic multilayer composites, Scr. Mater. 50 (6) (2004) 775–779.

[13] Z. Zhang, X. Gu, D. Holec, M. Bartosik, P.H. Mayrhofer, H.P. Duan, Superlattice-induced oscillations of interplanar distances and strain effects in the CrN/AlN system, Phys. Rev. B 95 (15) (2017) 155305.

[14] J.J. Roa, E. Jiménez-Piqué, R. Martínez, G. Ramírez, J.M. Tarragó, R. Rodríguez, L. Llanes, Contact damage and fracture micromechanisms of multilayered TiN/CrN coatings at micro- and nano-length scales, Thin Solid Films 571 (2014) 308–315.

[15] K. Bobzin, T. Brögelmann, N.C. Kruppe, M. Arghavani, J. Mayer, T.E. Weirich, Plastic deformation behavior of nanostructured CrN/AlN multilayer coatings deposited by hybrid dcMS/HPPMS, Surf. Coat. Technol. 332 (2017) 253–261.

[16] A. Azizpour, R. Hahn, F.F. Klimashin, T. Wojcik, E. Poursaeidi, P.H. Mayrhofer, Deformation and cracking mechanism in CrN/TiN multilayer coatings, Coatings 9 (6) (2019) 363.

[17] J. Buchinger, L. Löfler, J. Ast, A. Wagner, Z. Chen, J. Michler, Z.L. Zhang, P.H. Mayrhofer, D. Holec, M. Bartosik, Fracture properties of thin film TiN at elevated temperatures, Mater. Des. 194 (2020) 108885.

[18] N.J.M. Carvalho, J.T.M. De Hosson, Deformation mechanisms in TiN/(Ti,Al)N multilayers under depth-sensing indentation, Acta Mater. 54 (7) (2006) 1857–1862.

[19] S.J. Lloyd, A. Castellero, F. Giuliani, Y. Long, K.K. McLaughlin, J.M. Molina-Aldareguia, N.A. Stelmashenko, L.J. Vandeperre, W.J. Clegg, Observations of nanoindents via cross-sectional transmission electron microscopy: a survey of deformation mechanisms, Proceedings of the Royal Society A: Mathematical, Phys. Eng. Sci. 461 (2060) (2005) 2521–2543.

[20] Z. Chen, Y. Zheng, L. Löfler, M. Bartosik, G.K. Nayak, O. Renk, D. Holec, P.H. Mayrhofer, Z. Zhang, Atomic insights on intermixing of nanoscale nitride multilayer triggered by nanoindentation, Acta Mater. 214 (2021) 117004.

[21] M. Fallmann, Z. Chen, Z.L. Zhang, P.H. Mayrhofer, M. Bartosik, Mechanical properties and epitaxial growth of TiN/AlN superlattices, Surf. Coat. Technol. 375 (2019) 1–7.

[22] S. Uehara, T. Masamoto, A. Onodera, M. Ueno, O. Shimomura, K. Takemura, Equation of state of the rocksalt phase of III–V nitrides to 72 gpa or higher, J. Phys. Chem. Solids 58 (12) (1997) 2093–2099.

[23] L.H. Shen, X.F. Li, Y.M. Ma, K.F. Yang, W.W. Lei, Q.L. Cui, G.T. Zou, Pressure-induced structural transition in AlN nanowires, Appl. Phys. Lett. 89 (14) (2006) 141903.

[24] D. Holec, R. Rachbauer, D. Kiener, P.D. Cherns, P.M.F.J. Costa, C. McAleese, P.H. Mayrhofer, C.J. Humphreys, Towards predictive modeling of near-edge structures in electron energy-loss spectra of AlN-based ternary alloys, Phys. Rev. B 83 (16) (2011) 165122.

[25] D.G. Sangiovanni, L. Hultman, V. Chirita, I. Petrov, J.E. Greene, Effects of phase stability, lattice ordering, and electron density on plastic deformation in cubic TiWN pseudobinary transition-metal nitride alloys, Acta Mater. 103 (2016) 823–835.

[26] D.G. Sangiovanni, L. Hultman, V. Chirita, Supertoughening in B1 transition metal nitride alloys by increased valence electron concentration, Acta Mater. 59 (5) (2011) 2121–2134.

[27] M. Odén, H. Ljungcrantz, L. Hultman, Characterization of the induced plastic zone in a single crystal TiN(001) film by nanoindentation and transmission electron microscopy, J. Mater. Res. 12 (8) (2011) 2134–2142.

[28] L. Hultman, M. Shinn, P.B. Mirkarimi, S.A. Barnett, Characterization of misfit dislocations in epitaxial (001)-oriented TiN, NbN, VN, and (Ti,Nb) N film heterostructures by transmission electron microscopy, J. Cryst. Growth 135 (1) (1994) 309–317.

[29] Y. Wang, W. Wang, S. Fang, B. Dai, J. Zhu, The interface characteristics of TiN(100)/MgO(100) multilayer on oxidized Si(100) substrate via first-principle calculations and experimental investigation, Mol. Simul. 47 (7) (2021) 552–559.

[30] H.R. Azizpour A, F.F. Klimashin, T. Wojcik, E. Poursaeidi, P.H. Mayrhofer, Deformation and cracking mechanism in CrN/TiN multilayer coatings, Coatings 9 (2019) 363.